



Mesomechanical characteristics of rock failure under variable amplitude cyclic loading by DEM

Ze-han Liu¹ · Jin Yu² · Chong-hong Ren² · De-fu Zhu³ · Xiao-qin Chen¹

Received: 6 November 2022 / Accepted: 2 July 2023 / Published online: 14 July 2023
© Springer-Verlag GmbH Germany, part of Springer Nature 2023

Abstract

During the construction and application of underground engineering, rock materials are often subjected to cyclic loads with varying amplitudes. Although the mechanical properties of rock materials under cyclic loading have been extensively studied, the gradual process of internal crack propagation still needs further exploration and quantitative description. In this paper, the failure process of rock under monotonic loading and cyclic loading was analysed from macroscopic and microscopic perspectives using laboratory experiments and numerical simulations. Triaxial experiments and cyclic loading experiments with variable amplitudes were conducted on marble specimens under different confining pressures. Then, the experimental process was reproduced by numerical simulation using the discrete element method, and the process of rock failure was described quantitatively by defining the contact failure rate and damage density. In addition, the relationship between dissipated energy and crack propagation is discussed to some extent. The results show that based on the evolutions of the contact failure rate and damage density, the monotonic loading process can be more accurately divided into four stages. During the accelerating crack propagation stage, the cyclic load will generate more failure contacts beyond the direction of 70° to 110°, forming diffuse cracks and ultimately resulting in a bulging failure mode. The higher the confining pressure is, the greater the impact. The increment of the damage density is exponentially proportional to the increase in the cyclic stress amplitude ratio, while the relationship between the confining pressure condition coefficient and confining pressure follows a power function.

Keywords Marble · Cyclic loading · DEM · Crack extension · Dissipation energy

Introduction

It is well known that a rock mass usually suffers cyclic loading during geotechnical engineering activities, such as high slope excavation, tunnel excavation and dam storage and discharge. In addition, these activities involve problems such as construction disturbance of repeated loading and unloading, which would result in the accumulation and release of energy within the rock mass (Taheri et al. 2016; Ma et al. 2013; Bagde and Petroš 2005a, b, 2009; Song et al. 2012; Yu et al. 2020a, b). This will lead to the initiation, expansion, convergence and interaction of cracks inside the rock mass (Peng et al. 2015; Xie et al. 2011). Rock exhibits unique mechanical response characteristics under cyclic loading, which seriously affects the stability of the surrounding rock and severely threatens the safety of engineering technicians and equipment (Erarslan 2013, 2016; Liu and He 2012; Aghaei et al. 2012). Therefore, it is very important to study the damage and crack development processes of rock under cyclic loading.

✉ Jin Yu
bugyu0717@163.com

Ze-han Liu
591891989@qq.com

Chong-hong Ren
chren173@163.com

De-fu Zhu
hudefu@tyut.edu.cn

Xiao-qin Chen
469372202@qq.com

¹ School of Architecture and Civil Engineering, Xiamen Institute of Technology, Xiamen 361021, China

² Fujian Research Center for Tunneling and Urban Underground Space Engineering, Huaqiao University, Xiamen 361021, China

³ Key Laboratory of In-Situ Property-Improving Mining of Ministry of Education, Taiyuan University of Technology, Taiyuan 030024, China

The development of microdefects and new cracks in rock under the action of cyclic loading leads to rock deterioration and weakening. From the perspective of laboratory experiments, Xiao et al. (2010) compared and analysed the advantages and disadvantages of damage definition methods, such as the cumulative acoustic emission method, residual strain method and wave velocity method. The results showed that the residual strain method had clear physical significance and could reasonably consider the initial damage. On this basis, the concept of the average dynamic modulus was introduced to make this method better reflect the fatigue damage of rock under different loading conditions. However, this method requires many preliminary experiments to determine the material constants, and its application in engineering needs to be verified. Wang et al. (2018) studied the damage evolution of rock masses under cyclic loading with varying amplitudes and modified the damage method based on plastic strain. At the same time, the experimental process was analysed by acoustic emission. Li et al. (2019) studied the variation in the elastic modulus and residual deformation during variable-amplitude cyclic loading. Shen et al. (2020) used the acoustic emission method to study the effect of the lower stress limit on rock damage during the cyclic loading of sandstone. It is found that the damage caused by a single cycle can be inhibited with an increase in the lower limit of stress. Li et al. (2020) studied the influence of the loading rate on rock mass properties during cyclic loading and found that the higher the loading rate was, the larger the plastic strain and the smaller the residual strength. It was also considered that the failure of a rock mass can be predicted according to the change in energy and elastic energy index. Clearly, research on the damage evolution of cyclic loading is still mainly conducted through acoustic emission and energy dissipation. Although these methods can better represent the process of rock damage, it is difficult to directly observe the location of crack initiation and the trend of crack propagation. For this reason, more advanced test methods are applied to rock experiments. Ghamgosar and Erarslan (2016) used the Brazilian split test and numerical simulation method to study the development and closure of the fracture process zones (FPZ) of microcracks under static and repeated loading. The verification with X-ray microcomputed tomography observations showed that more microcracks were deduced under repeated loading due to the friction between grains. A smooth and luminous shear zone was formed under monotonic loading. Ghamgosar et al. (2017) also carried out different kinds of repeated loading experiments. Their results showed that the intensity decreased by approximately 30% due to step-by-step cyclic loading, and most of these high-density microcracks occurred in the FPZ zone. Wang et al. (2020) used X-ray microcomputed tomography to study the energy characteristics and crack development of rock under fatigue cyclic

loading and confining pressure unloading (FC-CPU) tests. The effect of the fatigue cycle on crack generation and the effect of unloading on crack size and density were revealed.

Although the emergence of computed tomography (CT) and other methods can help to this problem, it is still difficult to obtain more continuous data. With the development of computer technology, numerical simulation is increasingly applied to rock damage analysis. Zhou et al. (2019, 2020) studied the mechanical and deformation properties of rock materials under different frequencies, minimum stresses and amplitudes and single and multistage cyclic loads. On this basis, the constitutive relation of the rock dynamic response is established and verified using finite element numerical simulation. Cerfontaine et al. (2017) established a new constitutive model to study the volumetric strain of rock with the number of cycles by using the finite element method (FEM). However, natural rock masses usually contain weak structural planes such as cracks, joints and faults, which make it difficult to apply FEM and other continuum-based calculation methods. Moreover, this kind of method has difficulty simulating the failure and cracking of rock materials. For this reason, calculation methods based on discontinuous medium theory were developed (Tan et al. 2016). Tan et al. (2016) used block discrete elements and digital image processing (DIP) to jointly analyse the fracture process of granite in a Brazilian experiment and analysed the influence of rock inhomogeneity and microstructure on the fracture mode. Tan and Konietzky (2019) also used block discrete elements to study the stress, strain and seepage evolution of granite in triaxial compression tests. Liu et al. (2018) conducted experimental and particle discrete element numerical studies on brittle rocks through the Brazilian disc testing. The results showed that the cracks initiated at the centre of the specimen. As the cyclic loading proceeded, the cracks continued to grow in the vertical direction and eventually failed. Yu et al. (2020a, b) studied the evolutions law of the mechanical properties and permeability of weakly anisotropic sandstone in the process of fracturing from the perspective of the macroscopic and mesoscopic combination through triaxial experiments and the particle discrete element method (DEM). Saadat and Taheri (2019) used particle discrete elements to study the influence of particle size on the failure response of prefabricated fractured granite. Ma and Liu (2022) used the three-dimensional discontinuous deformation analysis (3D DDA) method to study the rockfall and fracture process of individual boulders and large rock masses under different geometric slope conditions, providing a basis for the development of disaster prevention strategies in practical engineering.

The current discrete element numerical simulation is mainly based on triaxial experiments or Brazilian splitting experiments. The crack initiation and propagation in the cyclic loading process need further study. However,

Potyondy and Cundall (2014) noted that when a particle discrete element numerical specimen was calibrated in terms of uniaxial strength, its strength in the process of triaxial numerical simulation was meagre. To investigate the difference between the damage accumulation process and the mesoscopic mechanism of the rock under monotonous loading and cyclic loading, first, laboratory triaxial experiments and cyclic loading experiments to variable loading amplitudes were conducted on the marble specimens. From a macroscopic perspective, the differences in the mechanical properties and failure modes of marble under different loading conditions were analysed. Then, a discrete element numerical model was established based on the laboratory experimental results. The numerical simulation results were compared with the experimental results to verify the reliability of the numerical model and reveal the differences in the process of internal crack propagation in marble specimens from a microscopic perspective. The corresponding relationship between dissipated energy and crack extension was also discussed.

Laboratory experiments

Specimen preparation

The rock specimens are white coarse-grained marble, which is homogeneous, with no impurities and fewer cracks. The average density of the specimens is 2602 kg/m³. According to the recommendations of the International Society for Rock Mechanics (ISRM), the specimens were processed into standard cylinders with a diameter of 50 mm and a height of 100 mm. The flatness of the processed specimen end face was within 0.02 mm, and the diameter error was less than 0.03 mm.

Experimental apparatus and method

A TFD-2000/D type electrohydraulic servo triaxial test machine was used in this study. The maximum confining pressure is 100 MPa, the maximum axial pressure is 2000 kN, and the measuring accuracy of the stress sensor is 0.01 kN. An axial extensometer and a circumferential chain extensometer were adopted for deformation measurement. The maximum ranges are 10 mm and 3 mm, respectively, and the measurement resolution is 0.0001 mm. The control system was an EDC digital servo controller, which can realize different control types, such as axial stress control, axial strain control, hoop strain control and hoop stress control.

Five groups of tests were set up according to different confining pressures: 0 MPa (uniaxial condition), 5 MPa, 10 MPa, 15 MPa and 20 MPa. There were five specimens for each group, with two specimens subjected to monotonic

loading and the other three specimens subjected to cyclic loading. Strain control was used during loading with a loading rate of 0.03 mm/min. Since unloading might start near the peak stress point, in which the specimen might fail and strain control was no longer suitable, stress control was used during unloading, with an unloading rate of 0.15 MPa/s. Referring to the peak stress from the monotonic loading test, the number of cycles was set to 5 in the cyclic loading tests with an equal-amplitude increment of stress (Fig. 1), and then the specimens were loaded until failure. Under the same confining pressure, the increasing amplitude was approximately 20% of the peak stress level in the monotonic loading test. The load was removed to 0 MPa after each target value was reached before starting the next loading cycles. As the rock specimens might fail before reaching the fifth loading target, the fifth unloading process was performed when the slope of the deformation curve was close to 0 or the present stress level was reached. The sixth loading process continued until the rock failed. The specific experimental results and analysis are presented in the next section.

Numerical simulation

After performing laboratory triaxial experiments and cyclic load experiments with variable loading amplitudes, a DEM numerical model was established by using Universal Distinct Element Code (UDEC) v7.0 (Itasca 2014) to further investigate the difference in crack development and failure mechanism between a rock mass under variable amplitude loading and unloading and that under monotonic loading.

DEM was proposed by Cundall and Strack (1979) in 1979 and has since been extensively studied and developed by

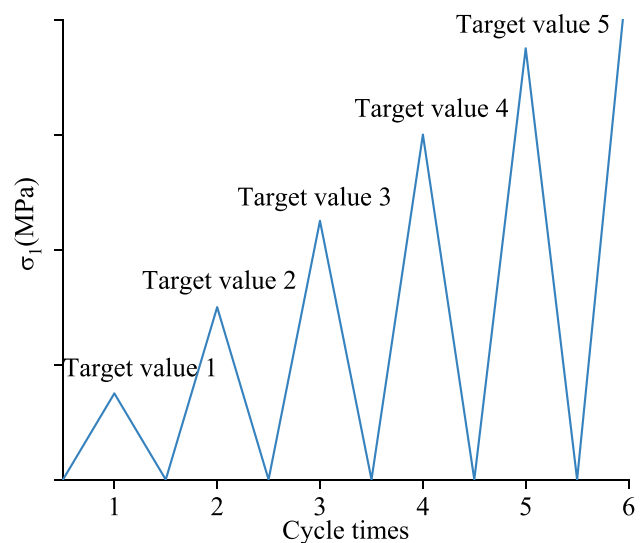


Fig. 1 Schematic diagram of loading and unloading

numerous scholars in the field of rock mechanics (Lin et al. 2020; He et al. 2021; Meng et al. 2021). DEM regards the problem domain (i.e. rock mass) as a collection of discrete blocks/particles, each with its own independent physical properties. The contact between each block is considered an interface between different objects, which means that the discontinuous parts are treated as boundary conditions. The motion of blocks is governed by Newton's second law, while the contact between blocks is described by a force–displacement relationship. The DEM updates the position, force and displacement of each block at each calculation step (Duan et al. 2020). At each calculation step, the contact between the blocks may fail and lose its load-bearing capacity when the stress in the shear or tensile direction exceeds the established strength. The force is then redistributed, causing other contacts to fail. Thus, the progressive failure process of rock is simulated (Woodman et al. 2021). Compared with continuous medium mechanics methods, such as the FEM, and other special algorithms such as special joint elements (Goodman 1976) and discrete fracture networks (Jing and Stephansson 2007), DEM have inherent advantages in simulating the initiation and propagation of rock cracks (Tan et al. 2016).

To date, mature discrete element software can be divided into particle-based discrete element software, such as Particle Flow Code (PFC) (Mehranpour and Kulatilake 2017) and MatDEM (Liu et al. 2021), and block-based discrete element software, such as UDEC. However, in the numerical simulation of rock materials using PFC, the tensile strength presented by the numerical specimens is exceptionally high (Cho et al. 2007). Although the use of 'cluster logic'-generated models can solve this problem to some extent (Cho et al. 2007; Potyondy and Cundall 2014), this modelling method involves some microscopic parameters that have no physical meaning. In addition, considering that the smallest unit of rock specimens is more similar to a polyhedral block than a sphere, Lorig and Cundall (1989) built the Voronoi program into UDEC, which can quickly discretize numerical specimens into a collection of polygonal blocks. In view of the above considerations, UDEC was finally selected to replicate the laboratory experiment process.

DEM model establishment

First, one intact numerical specimen was generated. The numerical specimen size is the same as that of the laboratory test, with a width of 50 mm and a height of 100 mm. Then, two rigid splints were generated at the top and bottom of the numerical specimen. There is no friction between the rigid splint and the specimen. Finally, the numerical specimen was discretized into convex polygonal blocks using the built-in Voronoi program. Considering the calculation accuracy and calculation efficiency of the model, the average side length of the final block was selected to be 2 mm.

The divided convex polygonal blocks were rigid and only had a density attribute of 2602 (kg/m³), which was the same as the average density of the test specimen. The contact between blocks adopted the Mohr–Coulomb point contact constitutive model. The microscopic parameters include contact normal stiffness Jkn , contact shear stiffness Jks , contact cohesion strength c^c , contact friction angle φ^c , contact tensile strength σ_t^c and contact dilatancy angle ψ^c . The maximum tensile strength of contact was determined by the contact tensile strength σ_t^c , and its maximum shear strength was determined by the contact cohesion strength c_c and contact friction angle φ^c . Contact failure occurred when the contact force exceeded the set maximum tensile or shear strength. The expansion behaviour after contact failure was controlled by the contact dilatancy angle ψ^c . Because each block is rigid, the macroscopic mechanical properties of the numerical specimens depend entirely on the choice of contact parameters. First, the microscopic parameters of the numerical specimen were verified based on laboratory uniaxial loading experimental data. The contact normal stiffness and contact shear stiffness were preliminarily calculated according to the method in the UDEC manual (Itasca 2014). Other parameters were selected according to the microcontact parameter calibration method mentioned by Kazerani and Zhao (2010). It is well known that rock is a typical heterogeneous material. As a result, the mesoscopic mechanical parameter distribution of the numerical specimen will be more complex. To simulate the inhomogeneity within the rock, the microscopic contact parameters were assigned Weibull distributions (Xu et al. 2020):

$$f(a) = \frac{m}{a_0} \left(\frac{a}{a_0}\right)^{m-1} e^{-\left(\frac{a}{a_0}\right)^m} \quad (1)$$

where a is the mesoscopic parameter and a_0 is the average mesoscopic parameters value. m is the shape parameter of the Weibull distribution. However, the built-in parameter assignment method of UDEC cannot accurately assign the microscopic parameters with Weibull distributions to the contact points, so it uses Fish statement programming to achieve this. To ensure that the numerical specimen maintains quasi-static equilibrium without a strength increase or unexpected mechanical response during the simulation process, damping should be applied at each computational step. Sinha et al. (2022) noted that the damping mode had no significant effect on the mechanical response of the numerical model at the specimen scale. However, considering that the cyclic load will be simulated, the block velocity will change significantly, so the 'local' damping mode was adopted. After the preliminary determination of the microscopic parameters, the method proposed by Stavrou and Murphy (2018) was used to inversely calculate and iterate the microscopic parameters. The final selection of microscopic parameters is shown in Table 1. The established numerical specimen is shown in Fig. 2.

Table 1 Contact parameter table

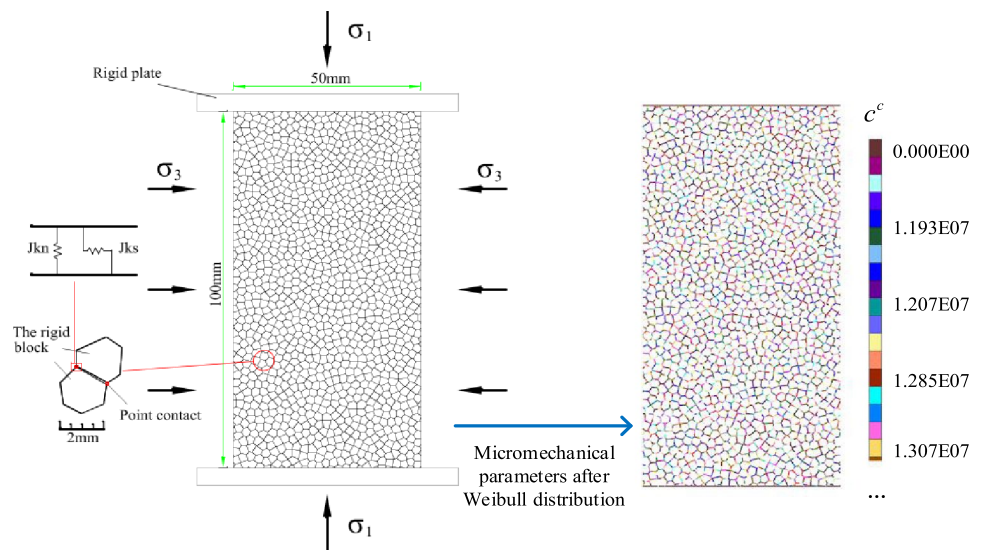
Input contact parameters			Macroscopic output parameters		
Normal stiffness of contact	Jkn (Pa/m)	4.45×10^8	Elastic modulus	E (GPa)	29.22
Shear stiffness of contact	Jks (Pa/m)	1.82×10^8	Poisson's ratio	μ	0.225
Friction angle of contact	φ^c (°)	25.5	Friction angle	φ (°)	25
Cohesion strength of contact	c^c (MPa)	24.24	Cohesion	c (MPa)	15.32
Tensile strength of contact	σ_t^c (MPa)	13.96			
Dilatancy angle of contact	ψ^c (°)	18			

The numerical model consists of 1302 blocks and 7864 contact points. During the loading process, the confining pressure is constant, the lower splint is fixed, and the specimen model is loaded by applying the upper splint a constant speed. The selected loading rate is 5×10^{-3} m/s.

Under uniaxial loading, the comparison between the numerical simulation and laboratory experiment results is shown in Fig. 3a, as indicated by the blue dashed and solid lines. The uniaxial compressive strength of the marble specimen and the numerical specimen is 48.71 MPa and 47.89 MPa, respectively, with a difference of only 1.68%. The elastic moduli are 29.56 GPa and 29.23 GPa, respectively, with a difference of 1.1%, indicating a good matching effect. Then, keeping the calibrated microparameters unchanged, laboratory triaxial compression experiments were simulated. The comparison results are shown in Fig. 3a and Table 2. The numerical results match well with the experimental results, and the selection of contact parameters is reasonable. That is, the numerical model can characterize the mechanical characteristics of this type of specimen. Figure 3b shows that the numerical results match the experimental results better under variable-amplitude cyclic loading. Both the numerical and experimental residual

strains increase with the upper cyclic stress ratio at a given confining pressure. As the confining pressure increases, the residual strain increases at the same upper limit stress ratio of the cyclic amplitude, and the hysteresis loop gradually becomes 'fuller'. In other words, the numerical model can characterize the mechanical properties of marble specimens under variable-amplitude cyclic loading. However, there are still some discrepancies between the simulation results and the experimental results. Although the variation in the obtained residual strain with the upper limit ratio of cyclic stress is similar, the experimental results are still quite different from the simulated results in terms of the residual strain. The numerical results also differ slightly from the simulation results in terms of the position of the peak for each cycle. After repeated consideration and discussion, it was determined that the reason for this difference should be that before the experiment, the batch of marble specimens was screened by density and wave velocity measurements, to make the specimens have a certain uniformity. However, the actual results show that the natural rock specimen still has large discreteness. For example, in Fig. 3b, the fourth loading peak and the fifth loading peak of the experimental stress–strain curve obviously do not conform

Fig. 2 DEM model schematic diagram



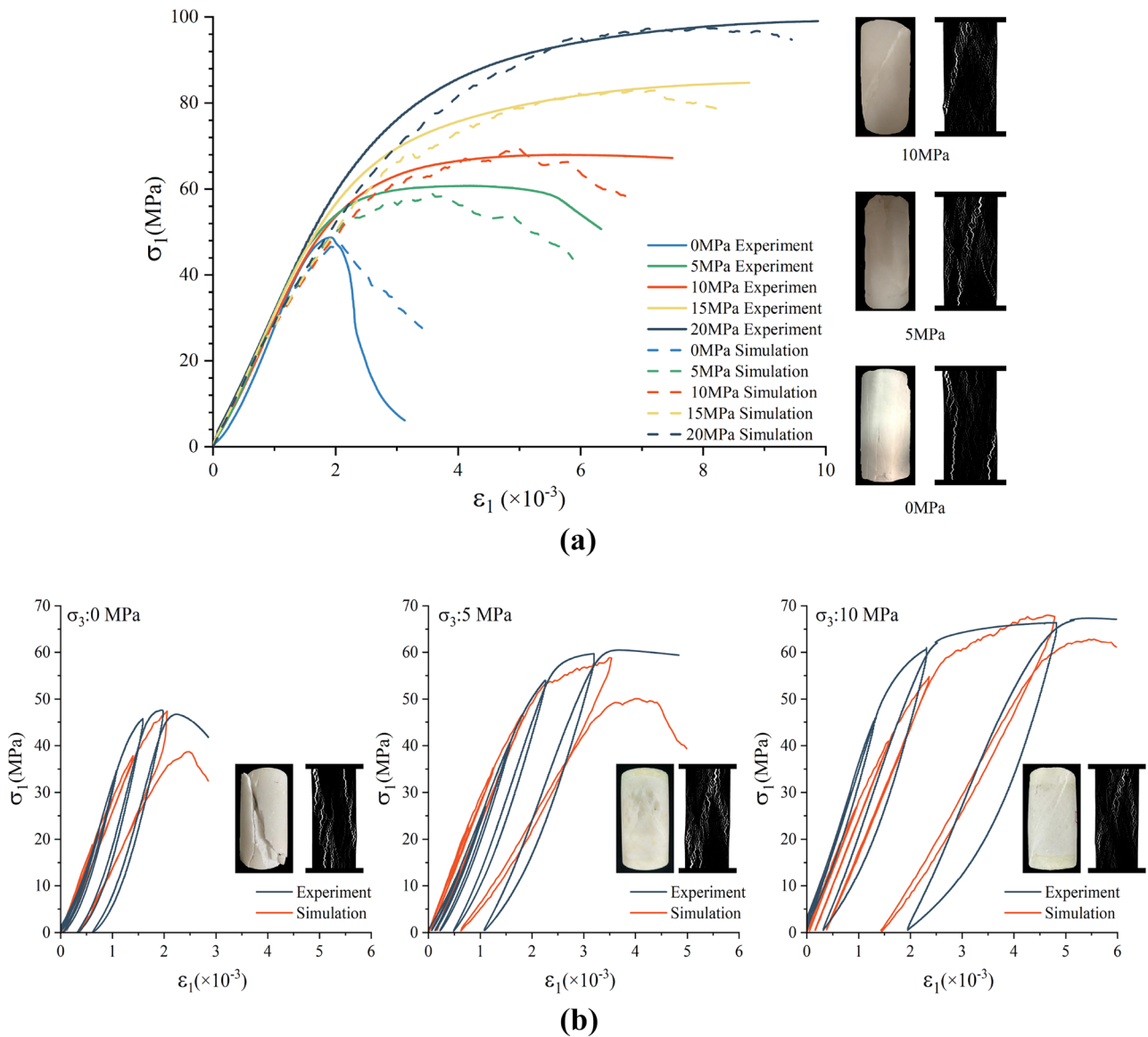


Fig. 3 Experimental and simulated stress–strain relationships under monotonic and cyclic loading conditions: **a** conventional triaxial stress–strain relationships under different confining pressures; **b** stress–strain relationships of cyclic loading under different confining pressures

to the expected experimental trend. Although the numerical specimens were discretized as Tyson polygon blocks and the Weibull distribution function was used to describe the internal inhomogeneity of the numerical specimens, the random

seeds used in the modelling were consistent, and the same numerical specimens were generated each time. This means that numerical specimens have better homogeneity and more reliable response patterns than natural rock specimens.

Table 2 Comparison of marble specimens with numerical specimens

Confining pressure (MPa)	Experimental peak strength (MPa)	Simulated peak strength (MPa)	Difference in peak strength (%)	Experimental elastic modulus (GPa)	Simulated elastic modulus (GPa)	Difference in elastic modulus (%)
5	60.53	59.13	2.31	31.18	29.23	6.25
10	67.77	69.56	−2.64	29.17	29.23	−0.20
15	83.65	82.96	0.82	30.73	29.23	4.89
20	97.81	97.45	0.36	30.30	29.23	3.55

The secant modulus of each loading in the stress–strain curve obtained by numerical simulation under a variable-amplitude cyclic load is statistically analysed and compared with the experimental results. The results are shown in Fig. 4.

As shown in Fig. 4, when the confining pressure is constant, the experimental secant modulus first increases and then decreases with increasing loading times, while the simulated secant modulus shows a nonlinear decreasing trend. The secant modulus of the first loading obtained from the experiment will change with the change in the confining pressure, and there is almost no regularity at all. However, the first secant modulus obtained by numerical simulation is kept at approximately 30 GPa, and the rate of decrease in the secant modulus increases with increasing confining pressure. This is because of the random distribution of voids and microcracks in natural rocks (Wang et al. 2022). Ren et al. (2022) believe that rock is in a competitive state of compaction and cracking during the failure process of loading. In the initial stage of variable-amplitude loading, many voids and microcracks are closed, and the rock tends to be dense, so the secant modulus of the first to third loading cycles shows an upwards trend. With the increase in the upper limit stress ratio and the number of cycles, the initial defects and new cracks continue to expand and converge, so the secant modulus shows a decreasing trend in the last two cycles. Even if the specimens are all taken from the same rock and screened, the internal defects still do not show a clear uniform distribution. With the change in confining pressure, the degree of compaction of voids and microcracks in a rock specimen also changes. This is why the secant modulus changes with the confining pressure during the first loading stage of the experiment. However, the blocks inside

the numerical specimens are in close contact with each other and will not be compacted during the loading process, so the secant modulus of the first loading stage under different confining pressures is maintained at approximately 30 GPa. As the loading continues, the internal contacts of the numerical specimen begin to fail, and the cracks gradually initiated and expanded. Therefore, the secant modulus of the numerical specimen decreases with increasing loading times.

Similarly, the variation in generalized Poisson’s ratio with loading times is shown in Fig. 5. Under the same confining pressure, the generalized Poisson’s ratio obtained by the experiment and simulation shows a trend of first being stable at and then increasing rapidly with the loading times. As the confining pressure increases, the generalized Poisson’s ratio obtained from the experiment increases. The generalized Poisson’s ratio obtained from the simulation under different confining pressures is stable at approximately 0.18 at the first loading and increases with increasing confining pressure after the second loading. The internal reason is similar to the change in the secant modulus.

However, that the purpose of numerical simulation is not to reproduce test data but to conduct a qualitative and quantitative analysis of data and phenomena that are difficult to monitor in the experiment after determining contact parameters based on standard laboratory test data.

Definition of damage variables

The connection between blocks can be regarded as a spring. When a contact point yields, the force will be redistributed (Huang et al. 2017), which may lead to the yielding of adjacent contact points and thus affect the macroscopic

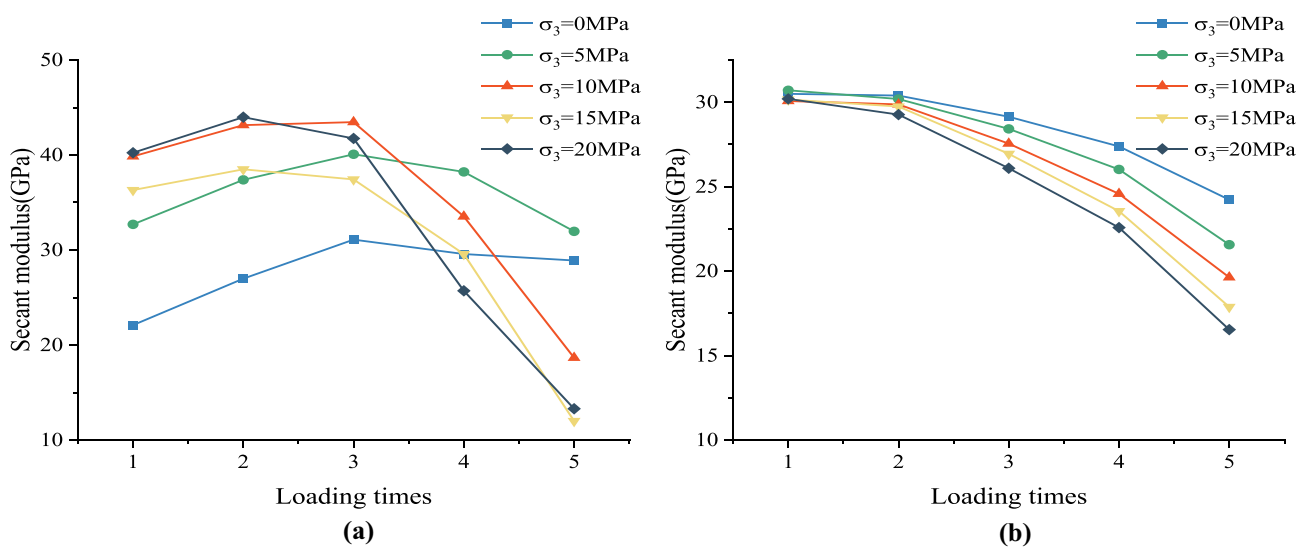


Fig. 4 The relationship between loading times and secant modulus: a experiment; b simulation

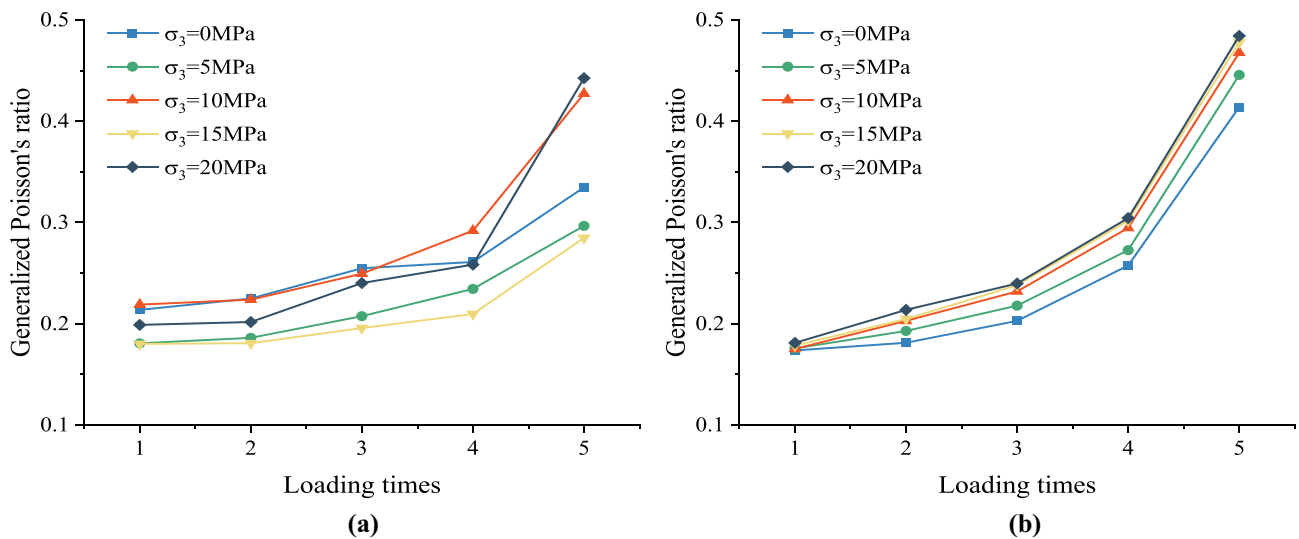


Fig. 5 The relationship between loading times and generalized Poisson’s ratio: **a** experiment; **b** simulation

mechanical properties of the specimen. Therefore, the number of failure contact points generated in the model was counted during the numerical simulation loading process to assist in describing the crack process of the specimen, as shown in Fig. 6b. The contact failure rate is defined as

$$D_{Mi} = \frac{C_{FP}}{C_{PP}} \tag{2}$$

where D_{Mi} is the contact failure rate, C_{FP} is the number of failure contact points, and C_{PP} is the number of preset contact points.

ImageJ software was used to binarize the displacement map obtained during the numerical simulation loading process, as shown in Fig. 6d. The crack area was captured and counted. The damage density is defined as

$$D_{Ma} = \frac{S_C}{S_C + S_{is}} \tag{3}$$

where D_{Ma} is the damage density, S_C is the crack area and S_{is} is the initial area of the specimen.

The simulation results are shown in Fig. 6, taking the confining pressure condition of 0 MPa as an example.

Damage evolution law

According to the various characteristics of the contact failure rate and damage density, the simulation curve of monotonic loading is successively divided into stage I (the elastic stage), stage II (the stable crack growth stage), stage III (the accelerating crack propagation stage) and stage IV (the postpeak failure stage), as shown in Fig. 6a. In stage I, the stress–strain relationship is linear, and the elastic modulus

stays the same. The contact failure rate is 0, the rate of increase in the damage density is approximately 0, and the increasing amount of damage density can be ignored. In this stage, no failure contact points are generated, and the contact expands uniformly. There is no crack in the specimen at this stage. In stage II, the stress–strain relationship exhibits a nonlinear change, and the elastic modulus decreases gradually. The contact failure rate increases steadily, and the damage density increases at a minimal low rate. At this stage, failure contact points start to be generated (Fig. 6b, a¹), and contact separation intensifies at the contact failure position (Fig. 6c, a¹). There are only a few cracks in the specimen (Fig. 6d, a¹). In stage III, the stress–strain relationship presents a rapid nonlinear change, and the elastic modulus continues to decrease. The rate of increase in the contact failure rate decreases gradually, while the damage density increases faster. In this stage, the number of failed contacts further increases (Fig. 6b, b¹), and the contact separation is further intensified at the failed contacts (Fig. 6c, b¹); thus, more cracks are formed (Fig. 6d, b¹). As the loading proceeds to the stress peak point, the increase in the number of failure contacts is no longer significant (Fig. 6b, c¹), and the contact separation increases rapidly in the upper left corner and lower right corner of the specimen (Fig. 6c, c¹), where the main cracks begins to form (Fig. 6d, c¹). In stage IV, the stress–strain curve starts to sag, and the bearing capacity of the specimen gradually decreases to zero. The contact failure rate tends to be stable, and the damage density increases at a tremendous rate. At this stage, the contact failure has little change compared with the peak stress (Fig. 6b, d¹), and the contact separation increases rapidly along with the initiation location of the main crack (Fig. 6c, d¹). Two main cracks are formed in the specimen (Fig. 6d, d¹).

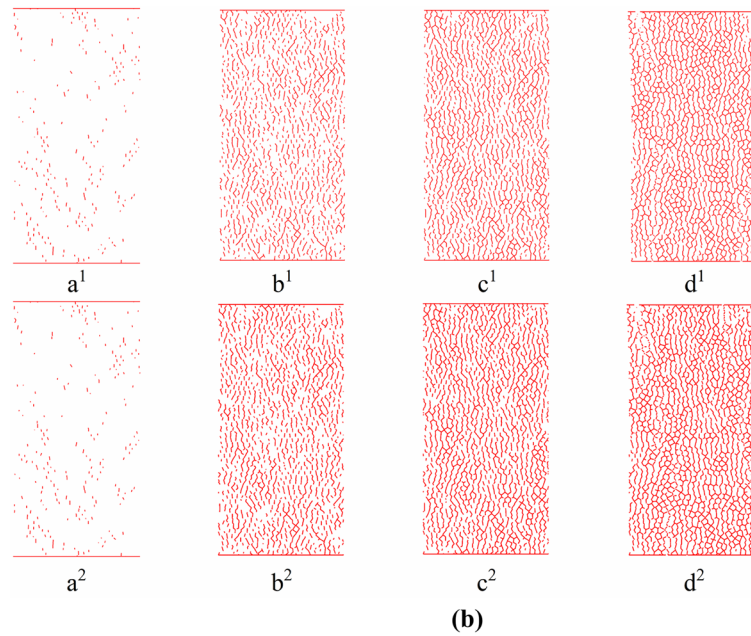
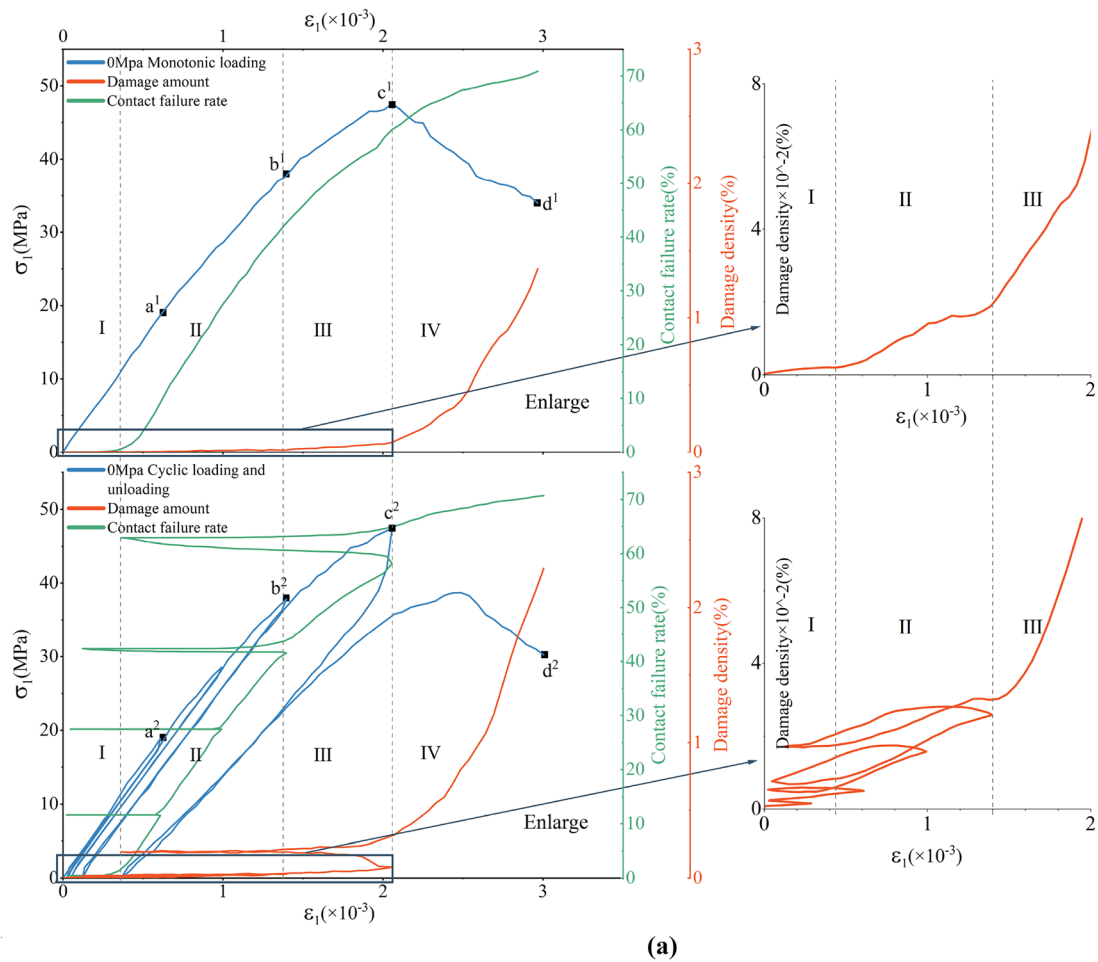


Fig. 6 Stress–strain relationship, damage evolution and crack evolution between monotonic loading and cyclic loading under 0 MPa confining pressure: **a** conventional triaxial stress–strain relations under different confining pressures; **b** evolution of failure contact under

monotonic loading and cyclic loading; **c** evolution of contact separation under monotonic loading and cyclic loading; **d** evolution of failure under monotonic loading and cyclic loading

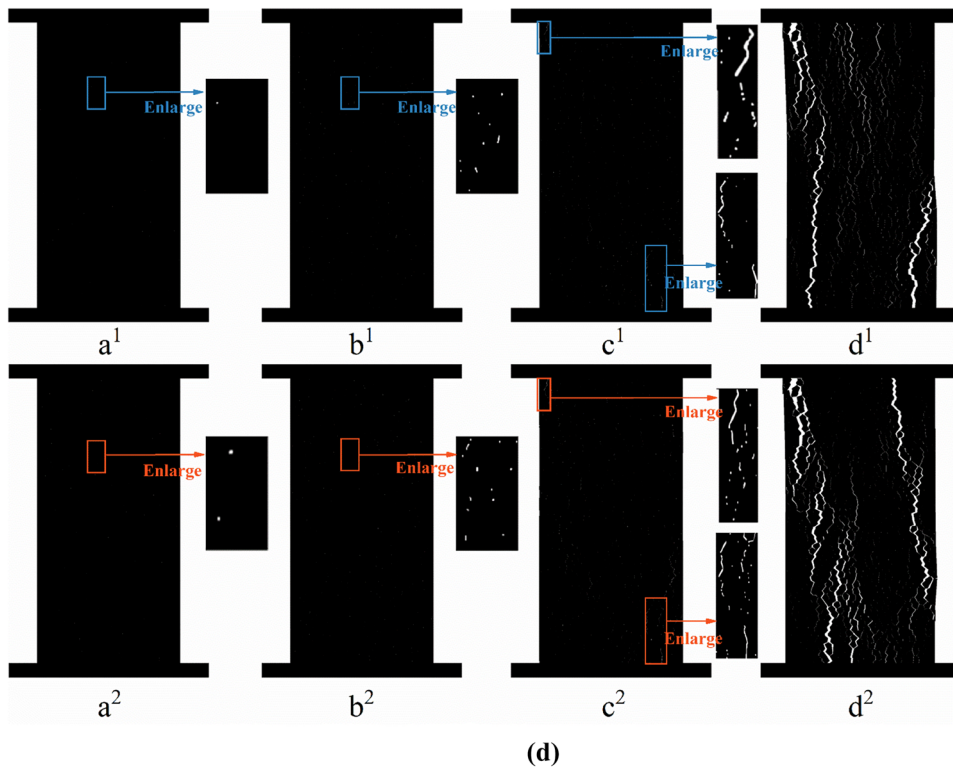
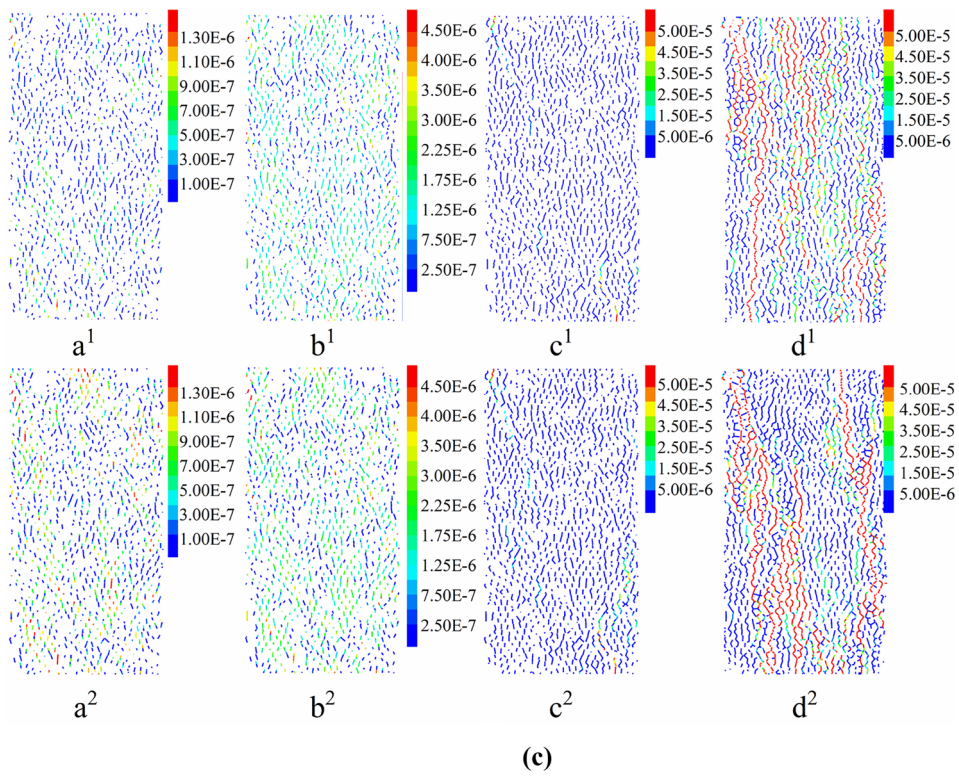


Fig. 6 (continued)

In the numerical simulation of variable-amplitude cyclic loading, the first cycle is completed in the elastic region, stage I. The cyclic load has no influence on the contact failure rate and damage density at this stage. The second and third cycles are in stable crack growth stage II. At this stage, the specimen does not produce more failure contacts under cyclic loading conditions than under monotonic loading (Fig. 6b, a²), so the contact failure rate does not change. However, the cyclic loading in this stage makes the contact separation more intense (Fig. 6c, a²) and the resulting crack wider (Fig. 6d, a²), which results in a slight increase in the damage density of cyclic loading compared to that of monotonic loading at this stage. The fourth and fifth cycles are in the accelerating crack propagation stage, stage III. At this stage, the number of failure contacts in specimens under cyclic loading is more than that under monotonic loading (Fig. 6b, b², c²), and the contact separation at partial failed contacts is more intense (Fig. 6c, b², c²). Therefore, more and wider cracks are generated in the specimen (Fig. 6d, b², c²). Thus, compared with the monotonic loading, cyclic loading in this stage causes more damage density. By comparing the results in postpeak failure stage IV, it is not difficult to see that there are more failure contacts due to the fourth and fifth cyclic loadings (Fig. 6b, d²). Because of the second to fourth cycles, the crack separation is more intense and more dispersed (Fig. 6c, d²). Because of the accumulation of failure contacts and damage density, the failure mode of the specimen changes. The analysis of the failure mode is described in detail below.

The failure contacts are divided into groups at an increment of 10°, and the failure contact lengths of each group are counted. The P_{21} formula in the two-dimensional case is used for calculation:

$$P_{21} = \frac{L}{A} \tag{4}$$

where L is the failure contact length and A is the area of the specimen.

The results are shown in Fig. 7. Clearly, in the initial loading process of monotonic loading ($\sigma_1 < 80\%$ peak stress), the specimen is in elastic stage I and the stable crack growth stage II. At these stages, the failure contacts mainly develop along the direction of 70° to 110°. With the increase in confining pressure, the contact failure expands faster in the direction of 70° to 110° and develops more obviously in other directions, which makes the curve of the plum blossom chart more ‘plump’. However, cyclic loading has little effect at this stage. As the monotonic loading continues ($80\% \leq \sigma_1 \leq 100\%$ peak stress), the specimen enters accelerating crack propagation stage III. At this stage, the failure contact develops slowly in the direction of 70° to 110° but rapidly in the other directions. The cyclic loading at this stage has little influence on the failure contacts in the direction from 70° to 110°, but more failure contacts are generated at other angles, and such influence is more obvious with increasing confining pressure.

The contact failure rate and damage density at the same stress ratio under different confining pressures are shown in Fig. 8.

Figure 8a shows that under the same confining pressure, when the stress ratio is less than 80%, the contact failure rate of the cyclic loading specimen is lower than that of the monotonic loading. When the stress ratio is greater than or equal to 80%, the contact failure rate of specimens under cyclic loading is greater than that under monotonic loading, and as the confining pressure increases, the difference in the contact failure rate increases. Figure 8b shows that under the same confining pressure, regardless of cyclic loading or monotonic loading, the damage density of the specimen is small when the stress ratio is less than 80%, but the damage density under cyclic loading is slightly larger than the damage density under monotonic loading. With the increase in the stress ratio, the difference in the damage density between the two stress paths gradually becomes obvious. As the confining pressure increases, the difference also becomes more obvious. In other words, cyclic loading produces more failure contact and cracks under higher confining pressures.

Fig. 7 The plum blossom diagram of failure contact development under different confining pressures

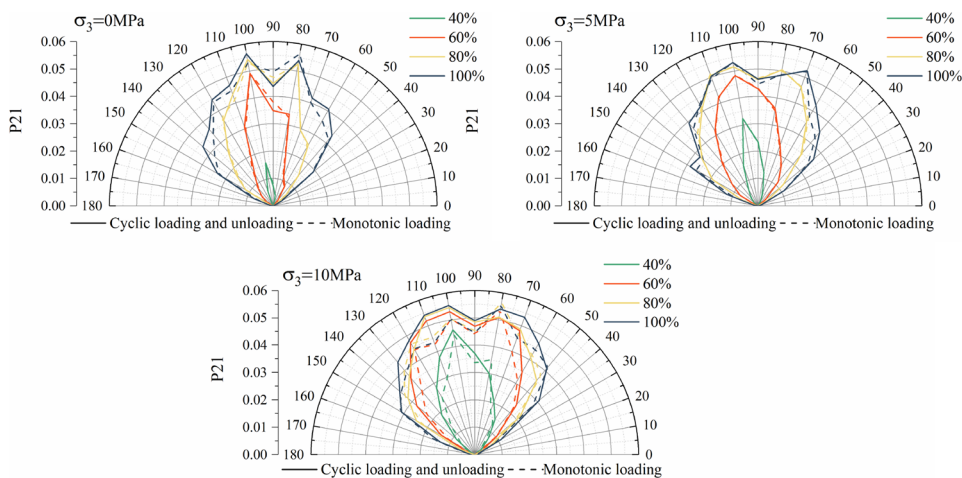
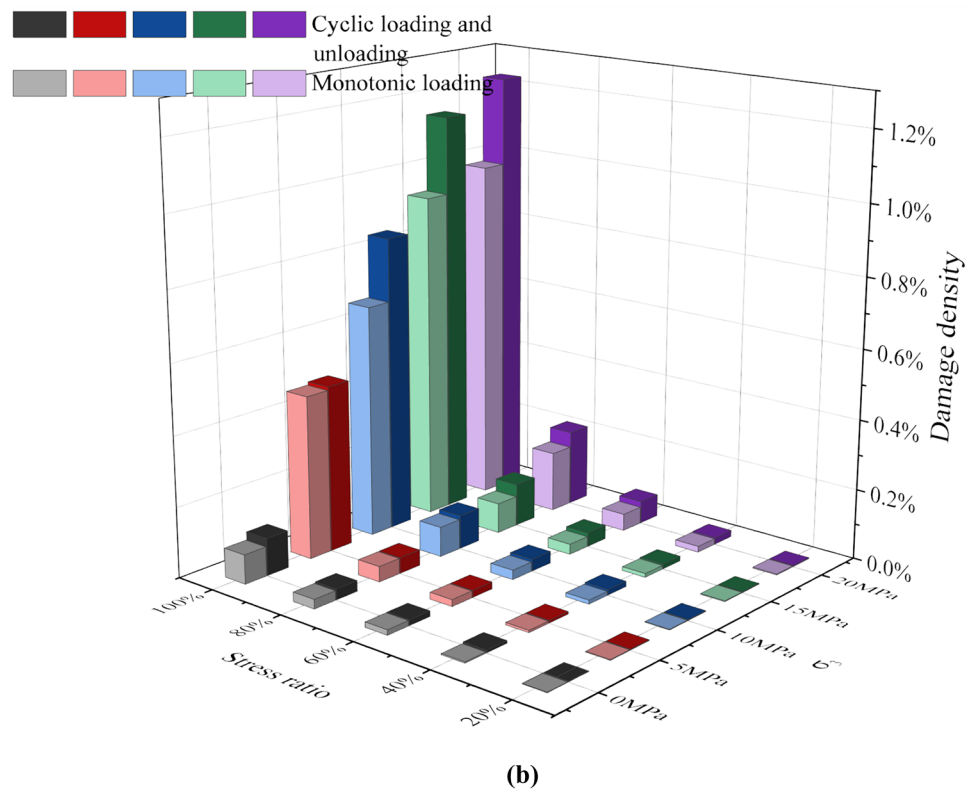
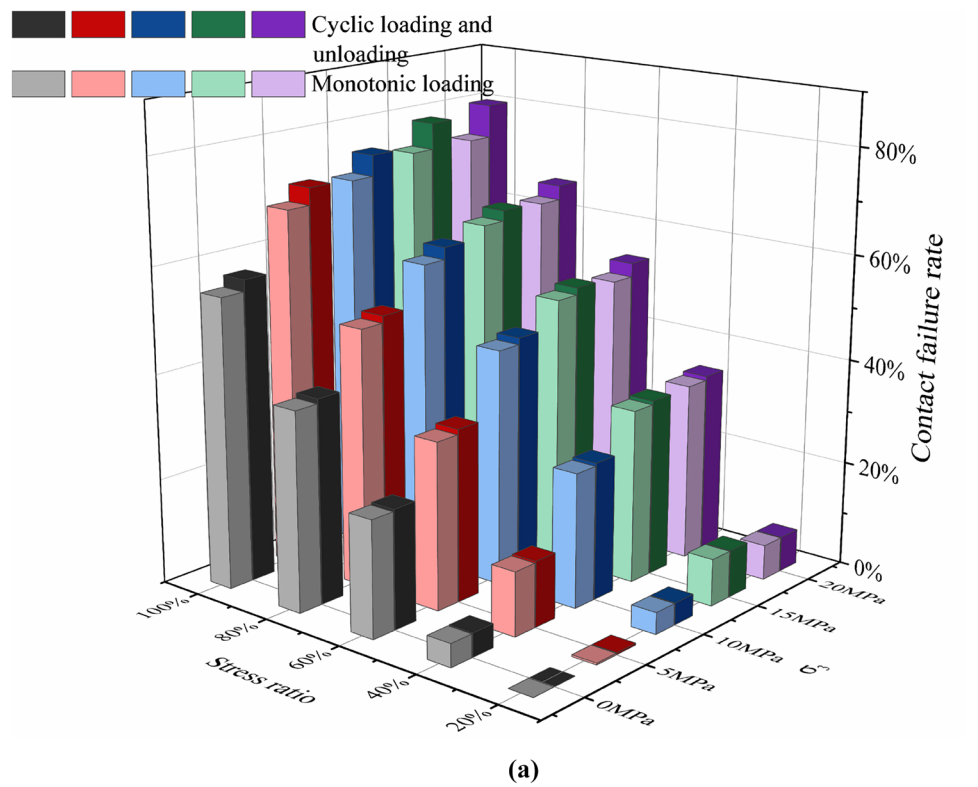


Fig. 8 Evolution of contact failure rate and damage density under different confining pressures: **a** evolution of contact failure rate under different confining pressures; **b** evolution of damage density under different confining pressures



Failure mode analysis

The failure modes of the two stress paths under different confining pressures are shown in Fig. 9. In Fig. 9, I, II, and III are the failure modes in the laboratory experiment, and i, ii, and iii are the failure modes in the numerical simulation.

Clearly, the failure mode results are basically consistent. Moreover, the numerical simulation can describe the failure mode of the specimen in more detail. When the confining pressure is 0 MPa, the specimen under monotonic loading shows splitting failure. Two main vertical cracks are formed in the specimen (Fig. 9a, i-1,2). However, the specimen exhibits shear failure under cyclic loading. The orientation of the main crack changes, and three vertical secondary cracks are generated below the main crack (Fig. 9b, i-1). The position of the other main crack changes (Fig. 9b, i-2), and a slight bulging failure occurs on the right side of the specimen (Fig. 9b, i-3). When the confining pressure is 5 MPa, the specimen shows shear failure under monotonic loading. There is an oblique main crack in the specimen (Fig. 9a, ii-1). However, the specimen exhibits conjugate shear failure under cyclic loading (Fig. 9b, ii-1,2). There are many secondary cracks in the specimen. Bulging failure appears on the middle part of the specimen (Fig. 9b, ii-3,4). When the confining pressure is 10 MPa, the specimen shows shear failure under monotonic loading, which is similar to that when the confining pressure is 5 MPa, and here is an oblique main crack in the specimen (Fig. 9a, iii-1). However, cyclic loading changes the location of the main crack to no longer penetrate the specimen (Fig. 9b, iii-1) and instead produce a new main crack that is inclined relative to the specimen axis (Fig. 9b, iii-2). In the middle part of the specimen, there is obvious bulging failure (Fig. 9b, iii-3,4).

The cyclic loading changes the failure mode of the specimen and causes bulging of the specimen. Moreover, the larger the confining pressure is, the more obvious the bulging phenomenon. This is because during the monotonic loading process, the rock specimen is affected by the inhomogeneity of the original microcracks, and the crack is formed in one direction first and then expands. Therefore, the specimen exhibits splitting failure or shear failure. In the process of cyclic loading, new cracks are generated throughout the specimen, which reduce the unevenness of the specimen. Therefore, the specimen presents conjugate shear failure mode and exhibits a bulging phenomenon.

Discussion

Incremental evolution of damage density

The incremental change in the damage density caused by the change in the upper limit ratio of cyclic stress under different

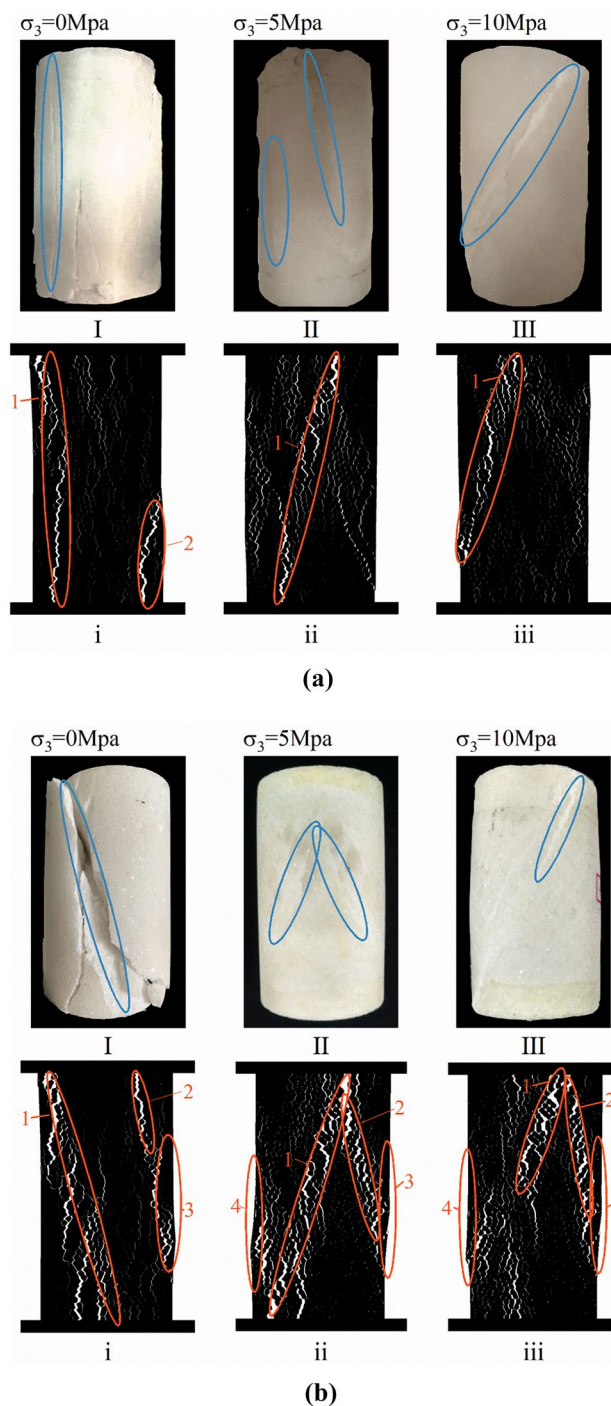


Fig. 9 Comparison of failure modes between cyclic loading specimens and monotonic loading specimens under different confining pressures: **a** failure modes of monotonic loading specimens under different confining pressures; **b** failure modes of cyclic loading specimens under different confining pressures

confining pressures is shown in Fig. 10. The increment of damage density caused by a single cycle can be calculated using Eq. (5):

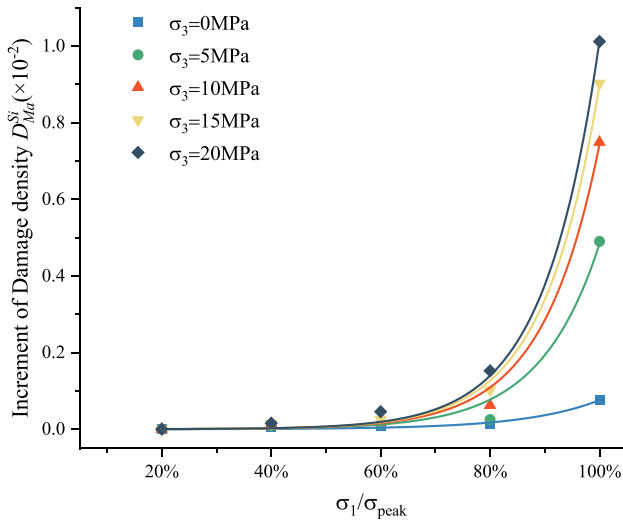


Fig. 10 Relation between the upper limit stress ratio of variable amplitude cyclic loading and D_{Ma}^{si}

$$D_{Ma}^{si} = D_{Ma}^n - D_{Ma}^{n-1} \tag{5}$$

where D_{Ma}^{si} represents the increment of the damage density caused by a single cycle and D_{Ma}^n is the damage density generated by the n th cycle. Clearly, before stage III, the change in the upper limit stress ratio has little effect on D_{Ma}^{si} . When the upper limit of cyclic stress enters the accelerating crack propagation stage, the change in the upper limit stress ratio has a significant effect on D_{Ma}^{si} . D_{Ma}^{si} has an exponential relationship with the upper limit ratio of cyclic stress, which can be fitted by Eq. (6).

$$D_{Ma}^{si} = R_{ock} \times a^{\sigma_{ceiling}} \tag{6}$$

where R_{ock} is the material constant; a is the confining pressure condition coefficient and $\sigma_{ceiling}$ is the upper limit ratio of cyclic stress. For this numerical specimen, R_{ock} is set to $5.30879e-5$. Values of confining pressure condition coefficient a and correlation coefficient R^2 under different confining pressures are shown in Table 3:

Table 3 shows that the correlation coefficients R^2 under different confining pressures are all above 0.98. This indicates that the selected equation accurately describes the relationship. The relationship between the confining pressure and a is shown in Fig. 11:

Table 3 Confining pressure condition coefficient and correlation coefficient

σ_3 (MPa)	Confining pressure condition coefficient a	Correlation coefficient R^2
0	1052.892	0.98664
5	9596.417	0.9847
10	14757.98	0.99445
15	17865.61	0.99864
20	20199.09	0.99861

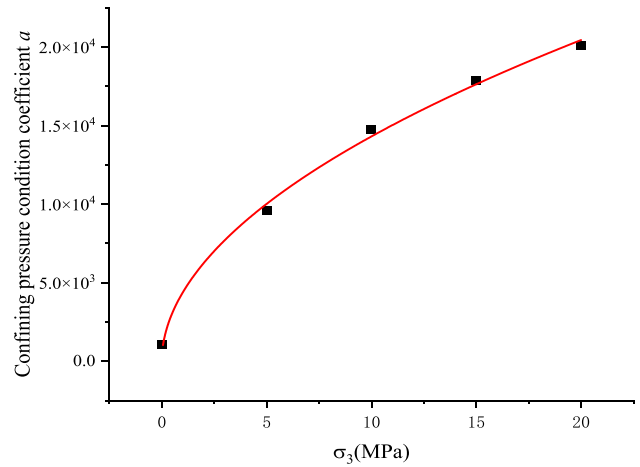


Fig. 11 The relationship between a and confining pressure

It can be seen from Fig. 11 that a increases along a power function with increasing confining pressure, so Eq. (7) can be used for fitting:

$$a = A \times \sigma_3^B \tag{7}$$

where A and B are fitting parameters. Under different confining pressure cyclic loads, the value of A is 4368.268, the value of B is 0.51514, the correlation coefficient R^2 is 0.98705, and the fitting effect is good.

Relationship between dissipated energy and crack propagation

Some scholars have suggested that rock deformation and failure reflects energy-driven instability, including energy absorption, evolution and dissipation; that is, the essence of rock failure is energy conversion (Xie et al. 2011; Park et al.

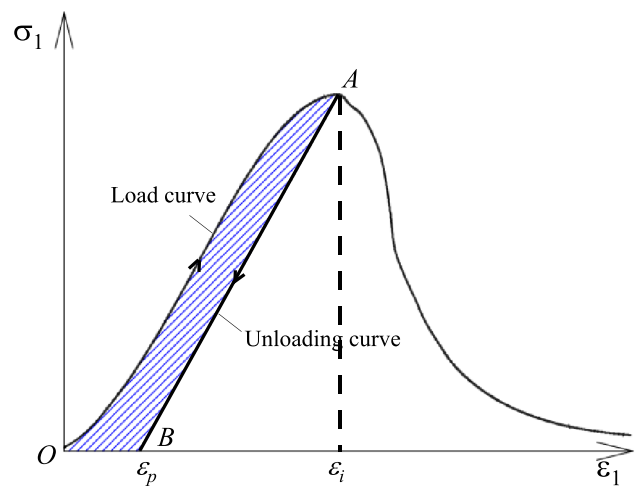
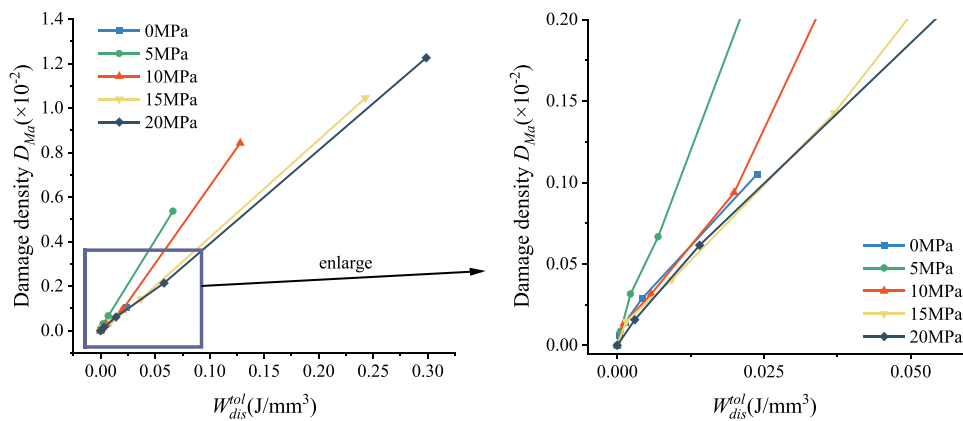


Fig. 12 Dissipated energy calculation principle

Fig. 13 Total dissipated energy–damage density relationship



2014; Ma et al. 2022). Based on this, many scholars have calculated the energy of rock through a stress–strain curve from cyclic loading experimentation, studied the energy evolution and established a corresponding damage evolution equation; this is a well-recognized approach (Liu et al. 2016; Meng et al. 2016). However, due to the limitation of experimental equipment and conditions, the evolution of internal cracks of rock specimens cannot be obtained directly during an experiment. How the dissipated energy calculated from the stress–strain curve corresponds to the evolution of the internal cracks in the specimen has not been fully discussed. The technology applied in this paper can obtain the parameters of the actual crack area while obtaining the stress–strain data. The above issues can be explored to some extent. The calculation method for dissipated energy is shown in Fig. 12 (Han et al. 2022).

From the perspective of energy, the area enclosed by the loading curve *OA* and the horizontal axis is the total input energy W_{tol} . The area enclosed by the unloading curve *AB* and the horizontal axis is the unloading recovery strain energy W_e . The shaded area in Fig. 12 is the dissipated energy under loading and unloading:

$$W_{dis} = W_{tol} - W_e = \int \sigma d\epsilon_i - \int \sigma d\epsilon_p \tag{8}$$

Here, we calculate the total dissipation energy for the *n*th cycle:

$$W_{dis}^{tol} = \sum W_{dis}^n \tag{9}$$

where W_{dis}^{tol} is the total dissipated energy under cyclic loading and W_{dis}^n is the dissipated energy calculated for the *n*th cycle. From this, the relationship between the total dissipated energy W_{dis}^{tol} and the damage density D_{Ma} can be obtained as shown in Fig. 13.

When the upper limit of the cyclic stress is small (i.e. the first to third cycles), the dissipated energy and the damage density show a nonlinear growth relationship. When

the upper limit of the cyclic stress is large (i.e. the third to fifth cycles), the dissipated energy seems to have a linear relationship with the damage density because when the upper limit stress is small, the dissipated energy of the rock is mainly caused by the friction between particles (blocks), and only a very small part of the dissipated energy is caused by the generation of cracks. With increasing upper limit stress, the specimen gradually completely fails. At this time, the energy dissipated due to the friction between particles (blocks) is negligible. Almost all the energy dissipated by the specimen is caused by the expansion of cracks. Of course, because the energy consumed by friction between particles is extremely difficult to measure, more advanced experimental methods are required to be verified in follow-up.

Conclusion

To study the trend of crack propagation in rock under variable-amplitude cyclic loading, the elastic parameters of rock and the process of crack propagation are analysed in detail by laboratory experiments and discrete element numerical simulation. The corresponding relationship between the dissipated energy and fracture area is discussed, and the conclusions are as follows

1. Under triaxial loading and cyclic variable-amplitude loading, the simulation results of the DEM numerical specimen calibrated by uniaxial experimental results are in good agreement with those of the laboratory experiments, indicating that the DEM numerical model can help establish the damage mechanism and intuitively capture the differences in crack propagation of rocks under different loading conditions. Additionally, in terms of the variation in elastic constants and peak stresses under different load conditions, numerical specimens demonstrate better uniformity than rock specimens.

2. The loading process can be more accurately divided into four stages according to the variation trends of the contact failure rate and damage density during monotonic loading. Compared with monotonic loading, cyclic loading not only affects the degree of contact separation, but also generates more/longer failure contacts in directions beyond 70° to 110°, ultimately resulting in a bulging failure mode of the specimen.
3. In cyclic variable-amplitude loading under various confining pressures, the increment of damage density is exponentially related to the upper limit ratio of cyclic stress. An exponential function expression is used for fitting, and the correlation coefficient R^2 is greater than 0.98 in all cases. After determining the material constant, the confining pressure condition coefficient in the relationship between the increase in damage density and the upper limit ratio of cyclic stress increases exponentially with increasing confining pressure. The correlation coefficient R^2 is 0.987, indicating a good fit.
4. When the upper limit of the cyclic stress is less than 80% of the peak stress, there is a nonlinear correspondence between the damage density and total dissipated energy. When the upper limit of the cyclic stress is greater than 80% of the peak stress, there is a linear correlation between the damage density and total dissipated energy. This may be related to the relationship between the energy dissipated by overcoming interparticle friction and that consumed by crack propagation.

Funding This work was supported by the National Natural Science Foundation of China (42077254, 51874144).

Data availability The data that support the findings of this study are available on request from the corresponding author, Jin Yu, upon reasonable request.

Declarations

Conflict of interest The authors declare no competing interests.

References

- Aghaei AA, Razeghi HR, Ghalandarzadeh A (2012) Effects of loading rate and initial stress state on stress-strain behavior of rock fill materials under monotonic and cyclic loading conditions. *Sci Iran* 19(5):1220–1235. <https://doi.org/10.1016/j.scient.2012.08.002>
- Bagde MN, Petroš V (2005a) Fatigue properties of intact sandstone samples subjected to dynamic uniaxial cyclical loading. *Int J Rock Mech Min Sci* 42(2):237–250. <https://doi.org/10.1016/j.ijrmms.2004.08.008>
- Bagde MN, Petroš V (2005b) waveform effect on fatigue properties of intact sandstone in uniaxial cyclical loading. *Rock Mech Rock Eng* 38(3):169–196. <https://doi.org/10.1016/j.ijrmms.2008.05.002>
- Bagde MN, Petroš V (2009) Fatigue and dynamic energy behaviour of rock subjected to cyclical loading. *Int J Rock Mech Min Sci* 46(1):200–209. <https://doi.org/10.1016/j.ijrmms.2008.05.002>
- Cerfontaine B, Charlier R, Collin F, Taiebat M (2017) Validation of a new elastoplastic constitutive model dedicated to the cyclic behaviour of brittle rock materials. *Rock Mech Rock Eng* 50(10):2677–2694. <https://doi.org/10.1007/s00603-017-1258-3>
- Cho NA, Martin CD, Sego DC (2007) A clumped particle model for rock. *Int J Rock Mech Min Sci* 44(7):997–1010. <https://doi.org/10.1016/j.ijrmms.2007.02.002>
- Cundall PA, Strack OD (1979) A discrete numerical model for granular assemblies. *Geotechnique* 29(1):47–65. <https://doi.org/10.1680/geot.1979.29.1.47>
- Duan K, Kwok CY, Zhang Q, Shang J (2020) On the initiation, propagation and reorientation of simultaneously-induced multiple hydraulic fractures. *Comput Geotech* 117:103226. <https://doi.org/10.1016/j.compgeo.2019.103226>
- Erarslan N (2013) A study on the evaluation of the fracture process zone in CCNBD rock samples. *Exp Mech* 53(8):1475–1489. <https://doi.org/10.1007/s11340-013-9750-5>
- Erarslan N (2016) Microstructural investigation of subcritical crack propagation and fracture process zone (FPZ) by the reduction of rock fracture toughness under cyclic loading. *Eng Geol* 208:181–190. <https://doi.org/10.1016/j.enggeo.2016.04.035>
- Goodman RE (1976) *Methods of geological engineering in discontinuous rocks*. West Group
- Ghamgosar M, Erarslan N (2016) Experimental and numerical studies on development of fracture process zone (FPZ) in rocks under cyclic and static loadings. *Rock Mech Rock Eng* 49(3):893–908. <https://doi.org/10.1007/s00603-015-0793-z>
- Ghamgosar M, Erarslan N, Williams DJ (2017) experimental investigation of fracture process zone in rocks damaged under cyclic loadings. *Exp Mech* 57(1):97–113. <https://doi.org/10.1007/s11340-016-0216-4>
- Han Y, Ma H, Cui H, Liu N (2022) The effects of cycle frequency on mechanical behavior of rock salt for energy storage. *Rock Mech Rock Eng* 55(12):7535–7545. <https://doi.org/10.1007/s00603-022-03040-1>
- He Q, Zhu L, Li Y, Li D, Zhang B (2021) Simulating hydraulic fracture re-orientation in heterogeneous rocks with an improved discrete element method. *Rock Mech Rock Eng* 54:2859–2879. <https://doi.org/10.1007/s00603-021-02422-1>
- Huang X, Liu Q, Liu B (2017) Experimental study on the dilatancy and fracturing behavior of soft rock under unloading conditions. *Int J Civ Eng* 15(6):1–28. <https://doi.org/10.1007/s40999-016-0144-9>
- Itasca (2014) UDEC version 6.0: theory and background. Itasca Consulting Group Inc., Minneapolis, Minnesota
- Jing L, Stephansson O (2007) Discrete fracture network (DFN) method. In *Developments in geotechnical engineering* 85:365–398. Elsevier
- Kazerani T, Zhao J (2010) Micromechanical parameters in bonded particle method for modelling of brittle material failure. *Int J Numer Anal Methods Geomech* 34(18):1877–1895. <https://doi.org/10.1002/nag.884>
- Li J, Hong L, Zhou K, Xia C, Zhu L (2020) Influence of loading rate on the energy evolution characteristics of rocks under cyclic loading and unloading. *Energies* 13(15):4003. <https://doi.org/10.3390/en13154003>
- Li T, Pei X, Wang D, Huang R, Tang H (2019) Nonlinear behavior and damage model for fractured rock under cyclic loading based on energy dissipation principle. *Eng Fract Mech* 206:330–341. <https://doi.org/10.1016/j.engfracmech.2018.12.010>
- Lin Q, Cao P, Meng J, Cao R, Zhao Z (2020) Strength and failure characteristics of jointed rock mass with double circular holes under uniaxial compression: insights from discrete element method modelling. *Theor Appl Fract Mech* 109:102692. <https://doi.org/10.1016/j.tafmec.2020.102692>
- Liu C, Liu H, Zhang H (2021) MatDEM-fast matrix computing of the discrete element method. *Earthq Res Adv* 1(3):100010. <https://doi.org/10.1016/j.eqrea.2021.100010>

- Liu E, He S (2012) Effects of cyclic dynamic loading on the mechanical properties of intact rock samples under confining pressure conditions. *Eng Geol* 125:81–91. <https://doi.org/10.1016/j.enggeo.2011.11.007>
- Liu XS, Ning JG, Tan YL, Gu QH (2016) Damage constitutive model based on energy dissipation for intact rock subjected to cyclic loading[J]. *Int J Rock Mech Min* 85:27–32. <https://doi.org/10.1016/j.ijrmms.2016.03.003>
- Liu YI, Dai F, Xu N, Zhao T, Feng P (2018) Experimental and numerical investigation on the tensile fatigue properties of rocks using the cyclic flattened Brazilian disc method. *Soil Dyn Earthq Eng* 105:68–82. <https://doi.org/10.1016/j.soildyn.2017.11.025>
- Lorig LJ, Cundall PA (1989) Modeling of reinforced concrete using the distinct element method. In: *Fracture of Concrete and Rock*, SEM-RILEM International Conference, Springer Verlag, pp 276–287
- Ma K, Liu G (2022) Three-dimensional discontinuous deformation analysis of failure mechanisms and movement characteristics of slope rockfalls. *Rock Mech Rock Eng* 55:275–296. <https://doi.org/10.1007/s00603-021-02656-z>
- Ma K, Ren F, Huang H, Yang X, Zhang F (2022) Experimental investigation on the dynamic mechanical properties and energy absorption mechanism of foam concrete. *Constr Build Mater* 342:127927. <https://doi.org/10.1016/j.conbuildmat.2022.127927>
- Ma L, Liu X, Wang M (2013) Experimental investigation of the mechanical properties of rock salt under triaxial cyclic loading. *Int J Rock Mech Min Sci* 62:34–41. <https://doi.org/10.1016/j.ijrmms.2013.04.003>
- Mehranpour MH, Kulatilake PH (2017) Improvements for the smooth joint contact model of the particle flow code and its applications. *Comput Geotech* 87:163–177. <https://doi.org/10.1016/j.compgeo.2017.02.012>
- Meng F, Pu H, Sasaoka T, Shimada H, Liu S, Dintwe TK, Sha Z (2021) Time effect and prediction of broken rock bulking coefficient on the base of particle discrete element method. *Int J Min Sci Technol* 31(4):643–651. <https://doi.org/10.1016/j.ijmst.2021.05.004>
- Meng Q, Zhang M, Han L, Pu H, Nie T (2016) Effects of acoustic emission and energy evolution of rock specimens under the uniaxial cyclic loading and unloading compression. *Rock Mech Rock Eng* 49(10):3873–3886. <https://doi.org/10.1007/s00603-016-1077-y>
- Park JW, Park D, Ryu DW, Choi BH, Park ES (2014) Analysis on heat transfer and heat loss characteristics of rock cavern thermal energy storage. *Eng Geol* 181:142–156. <https://doi.org/10.1016/j.enggeo.2014.07.006>
- Peng R, Ju Y, Wang JG (2015) Energy dissipation and release during coal failure under conventional triaxial compression. *Rock Mech Rock Eng* 48(2):509–526. <https://doi.org/10.1007/s00603-014-0602-0>
- Potyondy DO, Cundall PA (2014) A bonded-particle model for rock. *Int J Rock Mech Min Sci* 41(8):1329–1364. <https://doi.org/10.1016/j.ijrmms.2004.09.011>
- Ren C, Yu J, Liu X, Zhang Z, Cai Y (2022) Cyclic constitutive equations of rock with coupled damage induced by compaction and cracking. *Int J Min Sci Technol*. <https://doi.org/10.1016/j.ijmst.2022.06.010>
- Saadat M, Taheri A (2019) A numerical approach to investigate the effects of rock texture on the damage and crack propagation of a pre-cracked granite. *Comput Geotech* 111:89–111. <https://doi.org/10.1016/j.compgeo.2019.03.009>
- Shen R, Chen T, Li T, Li H, Fan W, Hou Z, Zhang X (2020) Study on the effect of the lower limit of cyclic stress on the mechanical properties and acoustic emission of sandstone under cyclic loading and unloading. *Theor Appl Fract Mech* 108:102661. <https://doi.org/10.1016/j.tafmec.2020.102661>
- Sinha S, Aboulsleiman R, Walton G (2022) Effect of damping mode in laboratory and field-scale universal distinct element code (UDEC) models. *Rock Mech Rock Eng* 55(5):2899–2915. <https://doi.org/10.1007/s00603-021-02609-6>
- Song D, Wang E, Liu J (2012) Relationship between EMR and dissipated energy of coal rock mass during cyclic loading process. *Saf Sci* 50(4):751–760. <https://doi.org/10.1016/j.ssci.2011.08.039>
- Stavrou A, Murphy W (2018) Quantifying the effects of scale and heterogeneity on the confined strength of micro-defected rocks. *Int J Rock Mech Min Sci* 102:131–143. <https://doi.org/10.1016/j.ijrmms.2018.01.019>
- Taheri A, Royle A, Yang Z (2016) Study on variations of peak strength of a sandstone during cyclic loading. *Geomech Geophys Geo* 2(1):1–10. <https://doi.org/10.1007/s40948-015-0017-8>
- Tan X, Konietzky H (2019) Numerical simulation of permeability evolution during progressive failure of Aue granite at the grain scale level. *Comput Geotech* 112:185–196. <https://doi.org/10.1016/j.compgeo.2019.04.016>
- Tan X, Konietzky H, Chen W (2016) Numerical simulation of heterogeneous rock using discrete element model based on digital image processing. *Rock Mech Rock Eng* 49(12):4957–4964. <https://doi.org/10.1007/s00603-016-1030-0>
- Wang Q, Xu S, He M, Jiang B, Wei H, Wang Y (2022) Dynamic mechanical characteristics and application of constant resistance energy-absorbing supporting material. *Int J Min Sci Technol* 32(3):447–458. <https://doi.org/10.1016/j.ijmst.2022.03.005>
- Wang Y, Feng WK, Hu RL, Li CH (2020) Fracture evolution and energy characteristics during marble failure under triaxial fatigue cyclic and confining pressure unloading (FC-CPU) conditions. *Rock Mech Rock Eng* 53:1–20. <https://doi.org/10.1007/s00603-020-02299-6>
- Wang Z, Yao J, Tian N, Zheng J, Gao P (2018) Mechanical behavior and damage evolution for granite subjected to cyclic loading. *Adv Mater Sci Eng*. <https://doi.org/10.1155/2018/4312494>
- Woodman J, Ougier-Simonin A, Stavrou A, Vazaios I, Murphy W, Thomas ME, Reeves HJ (2021) Laboratory experiments and grain based discrete element numerical simulations investigating the thermo-mechanical behaviour of sandstone. *Geotech Geol Eng* 2021:1–21. <https://doi.org/10.1007/s10706-021-01794-z>
- Xiao JQ, Ding DX, Jiang FL, Xu G (2010) Fatigue damage variable and evolution of rock subjected to cyclic loading. *Int J Rock Mech Min Sci* 47:461–468. <https://doi.org/10.1016/j.ijrmms.2009.11.003>
- Xie H, Li L, Ju Y (2011) Energy analysis for damage and catastrophic failure of rocks. *Sci China-Technol* 54(1):199–209. <https://doi.org/10.1007/s11431-011-4639-y>
- Xu Y, Yao W, Xia K (2020) Numerical study on tensile failures of heterogeneous rocks. *J Rock Mech Geotech* 12(1):50–58. <https://doi.org/10.1016/j.jrmge.2019.10.002>
- Yu J, Liu G, Cai Y, Zhou J, Liu S, Tu B (2020a) Time-dependent deformation mechanism for swelling soft-rock tunnels in coal mines and its mathematical deduction. *Int J Geomech* 20(3):04019186. [https://doi.org/10.1061/\(ASCE\)GM.1943-5622.0001594](https://doi.org/10.1061/(ASCE)GM.1943-5622.0001594)
- Yu J, Yao W, Duan K, Liu X, Zhu Y (2020b) Experimental study and discrete element method modeling of compression and permeability behaviors of weakly anisotropic sandstones. *Int J Rock Mech Min Sci* 134:104437. <https://doi.org/10.1016/j.ijrmms.2020.104437>
- Zhou Y, Sheng Q, Li N, Fu X (2019) Numerical investigation of the deformation properties of rock materials subjected to cyclic compression by the finite element method. *Soil Dyn Earthq Eng* 126:105795. <https://doi.org/10.1016/j.soildyn.2019.105795>
- Zhou Y, Sheng Q, Li N, Fu X (2020) Numerical analysis of the mechanical properties of rock materials under tiered and multi-level cyclic load regimes. *Soil Dyn Earthq Eng* 135:106186. <https://doi.org/10.1016/j.soildyn.2020.106186>

Springer Nature or its licensor (e.g. a society or other partner) holds exclusive rights to this article under a publishing agreement with the author(s) or other rightsholder(s); author self-archiving of the accepted manuscript version of this article is solely governed by the terms of such publishing agreement and applicable law.